G protein–coupled estrogen receptor deficiency exacerbates demyelination through microglial ferroptosis

Received for publication, August 21, 2024, and in revised form, December 14, 2024 Published, Papers in Press, February 13, 2025,
https://doi.org/10.1016/j.jbc.2025.108312

Xiaojuan Mi[1,‡], Junjie Li[1,‡], Ziqi Feng[1,‡], Yanbo Liu[1], Chun Zhang[2], Yu Shao[1], Ting Wang[1], Zhilun Yang[1], Haowen Lv[1], and Juan Liu[1,3,*]

From the [1]School of Basic Medical Sciences, Ningxia Medical University, Yinchuan; [2]Key Laboratory of Craniocerebral Diseases of Ningxia Hui Autonomous Region, Ningxia Medical University, Yinchuan; [3]General Hospital of Ningxia Medical University, Yinchuan, Ningxia, China

Reviewed by members of the JBC Editorial Board. Edited by Elizabeth J. Coulson

Microglial activation is the initial pathological event that occurs in demyelination, a prevalent feature in various neurological diseases. G protein–coupled estrogen receptor 1 (GPER1), which is highly expressed in microglia, has been reported to reduce myelin damage. However, the precise molecular mechanisms involved remain unclear. In this study, the cuprizone (CPZ)-induced demyelination model was used to investigate the relationship between GPER1 and myelin sheath injury and its mechanism. The results demonstrated that *GPER1* deficiency exacerbated cognitive impairment in mice. Along with more severe myelin damage as well as fewer oligodendrocytes. Moreover, *GPER1* deficiency not only directly reduced the number of microglia in cuprizone mice but also caused iron ions overload in microglia of myelin debris induced *in vitro*. Transcriptomic, molecular biological, and morphological analyses revealed that microglial ferroptosis caused by *GPER1* deficiency contributes to the reduction of microglia number. In summary, these findings revealed that GPER1 can regulate demyelination through ferroptosis of microglia.

Demyelination of the central nervous system (CNS) is a pathological phenomenon associated with several neurological disorders, including multiple sclerosis (1), schizophrenia (2), and Alzheimer's disease (3, 4), which is characterized by the loss of myelin sheaths and myelin-supported oligodendrocytes (OLs). Cognitive dysfunction caused by demyelination has received increasing attention. Abnormalities in hippocampal structure and function play a key role in spatial learning and memory impairment in most demyelination-related disorders, which severely affect the prognosis of the disease and imposes a heavy physical, psychological, and economic burden on patients (1, 5–7). The extensive hippocampal demyelination induced by cuprizone (CPZ) model effectively mimics the hippocampal myelin damage observed under pathological conditions. Therefore, understanding the mechanism underlying myelin damage in the hippocampus could provide insight into addressing the cognitive impairment associated with these conditions.

Demyelination generates a large amount of myelin debris, which can selectively inhibit the differentiation of oligodendrocyte precursor cells (OPCs), leading to further accumulation of myelin debris and inhibition of myelin regeneration, thus exacerbating the pathological process of demyelination (8). Microglia, the scavengers of the CNS, facilitate myelin regeneration by clearing myelin fragments (9–11). Specifically, when microglia detect demyelination damage, they migrate to the site, remove myelin debris, and promote the differentiation of OPCs into OLs. These OLs encase demyelinated axons to complete remyelination (12, 13). Studies have shown that reduced microglia phagocytic activity delays recovery from demyelinating disease in humans and mice. However, the molecular mechanisms that regulate the microglial phagocytosis of myelin debris are unknown.

Ferroptosis is a critical form of cell death driven by with iron overload and lipid peroxidation (LPO) (14). Under demyelination pathology, iron-rich myelin debris creates an environment conducive to the onset of ferroptosis (15). Microglia retain more iron than do other cells due to the expression of multiple iron-related proteins (16–18). Under iron loading, activated microglia take up iron, and once the loading is exceeded, they exhibit ferroptosis (19), which correspondingly leads to an impaired ability to phagocytose myelin debris, thus exacerbating demyelination (20, 21). Studies have reported that G protein–coupled estrogen receptor 1 (GPER1) has a promoting effect on myelin regeneration (22) and is significantly expressed in microglia, which affecting their phagocytic capacity (23). Furthermore, activation of GPER1 attenuates cognitive dysfunction in mice with attention deficit disorder (24) and mice with subarachnoid hemorrhage (25). Recent studies have found that GPER1 inhibits cellular ferroptosis (26, 27). However, the role of GPER1 in microglia ferroptosis–mediated myelin damage is unknown. Here, we employed CPZ-treated and *GPER1* knockout (KO) mice to investigate its relationship with microglial ferroptosis, revealing the potential role of GPER1 in myelin damage and providing insight for the treatment of cognitive impairment in demyelinating diseases.

‡ These authors have contribute equally to this work.
* For correspondence: Juan Liu, 20070001@nxmu.edu.cn.

Results

GPER1 expression in the CPZ model was increased and mainly confined to microglia

Fast blue staining and myelin basic protein (MBP) immunofluorescence staining were conducted to assess the successful establishment of the CPZ model (Fig. 1, *A* and *B*). Consistent with a previous report (5), a significant decrease in the myelin content was observed in mice treated with CPZ. Western blotting analysis revealed the upregulation of GPER1 in the mice hippocampi of mice following CPZ treatment (Fig. 1, *C–E*). Immunofluorescence colabeling method was used to determine which cell executes the function of GPER1 in the CPZ model. The results indicated that GPER1 was mainly expressed in the $Iba1^+$ cells of the CPZ model. Moreover, the colabeled $Olig2^+/GPER1^+$ cells and $GFAP^+/GPER1^+$ cells showed much lower compared to $Iba1^+/GPER1^+$ cells (Fig. 1*F*). These findings confirmed the successful establishment of CPZ model.

GPER1 *KO exacerbated cognitive impairment in the CPZ mouse model*

GPER1 KO mice were used to investigate the role of GPER1 in the CPZ model. The new object recognition (NOR) and Morris water maze (MWM) experiments were conducted to assess the effects of GPER1 on cognition (Fig. 2*A*). In the NOR test, compared with wildtype (WT) mice, *GPER1* KO mice exhibited a substantial decrease in the time spent exploring unfamiliar objects. Furthermore, the *GPER1* KO/CPZ mice showed a further decline in exploration time compared with WT/CPZ mice (Fig. 2, *B* and *C*). In the MWM experiment, *GPER1* deficiency did not induce cognitive impairment under normal circumstances, while dampened the learning capacity of mice under the demyelinating conditions. In the positioning cruise test, *GPER1* KO/CPZ exhibited a greater amount of time devoted to exploring the platform in comparison to the WT/CPZ mice (Fig. 2, *D–F*). During the spatial exploration test, mice in the *GPER1* KO/CPZ group exhibited poorer memory performance, as evidenced by fewer platform crossings and longer time spent in the platform quadrant after platform removal. These findings support the exacerbated cognitive decline in the *GPER1* KO/CPZ group (Fig. 2*G*). Collectively, these results indicate that *GPER1* deletion worsens learning and cognitive impairments in demyelination.

GPER1 *KO accelerated myelin damage in the CPZ mouse model*

As the hippocampus is essential for cognition and is rich in myelin (28), RNA sequencing assay was performed to detect the change in gene expression in this region. Compared to the WT/CPZ mice, *GPER1* KO mice treated with CPZ exhibited downregulation of genes associated with myelination and myelin structure formation (*e.g.*, *MBP*, *Mag*, *Plp1*, *Mog*, *Mal*, *Mobp*, and *Cst7*) (Fig. 3*A*). Transmission electron microscopy (TEM) revealed the ultrastructural changes in the myelin sheath. Under normal circumstances, the myelin sheath displayed a dense lamellar structure, with no significant differences between the two genotypes. However, following CPZ treatment, the myelin lamellar structure of the myelinated nerve fibers in the hippocampus was lost in WT/CPZ mice. In the *GPER1* KO/CPZ group, more severe edema, vacuolar change, axonal separation, and lamellar separation were observed, compared with that in the WT/CPZ group (Fig. 3*B*). Quantitative analysis of TEM images showed that the number of myelinated axons in *GPER1* KO/CPZ mice decreased significantly more than that in WT/CPZ mice (Fig. 3*C*). In addition, Western blotting and immunofluorescence assays indicated a significant reduction in MBP protein levels in the hippocampus of *GPER1* KO/CPZ mice, compared with those in WT/CPZ mice (Fig. 3, *D* and *E*). Moreover, the substantial loss of MBP protein induced by *GPER1* KO resulted in more disorganized and clumpy myelin layers in demyelination mice (Fig. 3, *F* and *G*). Furthermore, we detected the expression of OPCs marker NG2 (Fig. S1, *A–D*) and OLs marker CNPase (Fig. S1, *E–H*) in the hippocampus. The result showed that *GPER1* KO further decreased the expression of CNPase and NG2 in CPZ model. Collectively, these findings indicate that *GPER1* deficiency exacerbates myelin damage by impairing the remyelination process.

GPER1 *KO reduced the accumulation of Iba1-positive microglia in the CPZ mouse model*

To determine the functions of GPER1 in microglia, we first measured Iba1 levels in the CPZ model. Consistent with previous studies (12, 29), immunohistochemistry indicated an increase in the number of $Iba1^+$ cells (a microglial marker) in WT mice following CPZ treatment. These $Iba1^+$ cells in the WT/CPZ group were characterized by enlarged cell bodies and more numerous and thicker processes. Interestingly, the number of $Iba1^+$ cells in the hippocampus in the *GPER1* KO/CPZ group was significantly lower than that in the WT/CPZ group (Fig. 4, *A* and *B*). This phenomenon and the observed increased colabeling of GPER1 and microglia after CPZ treatment (Fig. 1*F*) indicate that the reduced number of microglia in the *GPER1* KO/CPZ group may have contributed to the worse pathology and greater cognitive impairment observed in this model.

GPER1 *KO accelerated ferroptosis in the CPZ mouse model*

Given that myelin debris is rich in iron and that microglia play a role in iron storage (17, 19), we measured the iron content in tissues after demyelination. Fig. 5*A* indicates an increase in free iron concentration in the brain of two phenotype mice following myelin injury, particularly in the *GPER1* KO mice. Additionally, *GPER1* KO/CPZ mice further increased malondialdehyde (MDA) and LPO production compared with that in WT/CPZ mice (Fig. 5, *B* and *C*). Using Perls' staining, we found iron deposition in the hippocampal cornu ammonis (CA)1 and CA3 regions of both genotype mice. Notably, the *GPER1* KO/CPZ mice showed more iron deposition after CPZ treatment, than did WT/CPZ mice

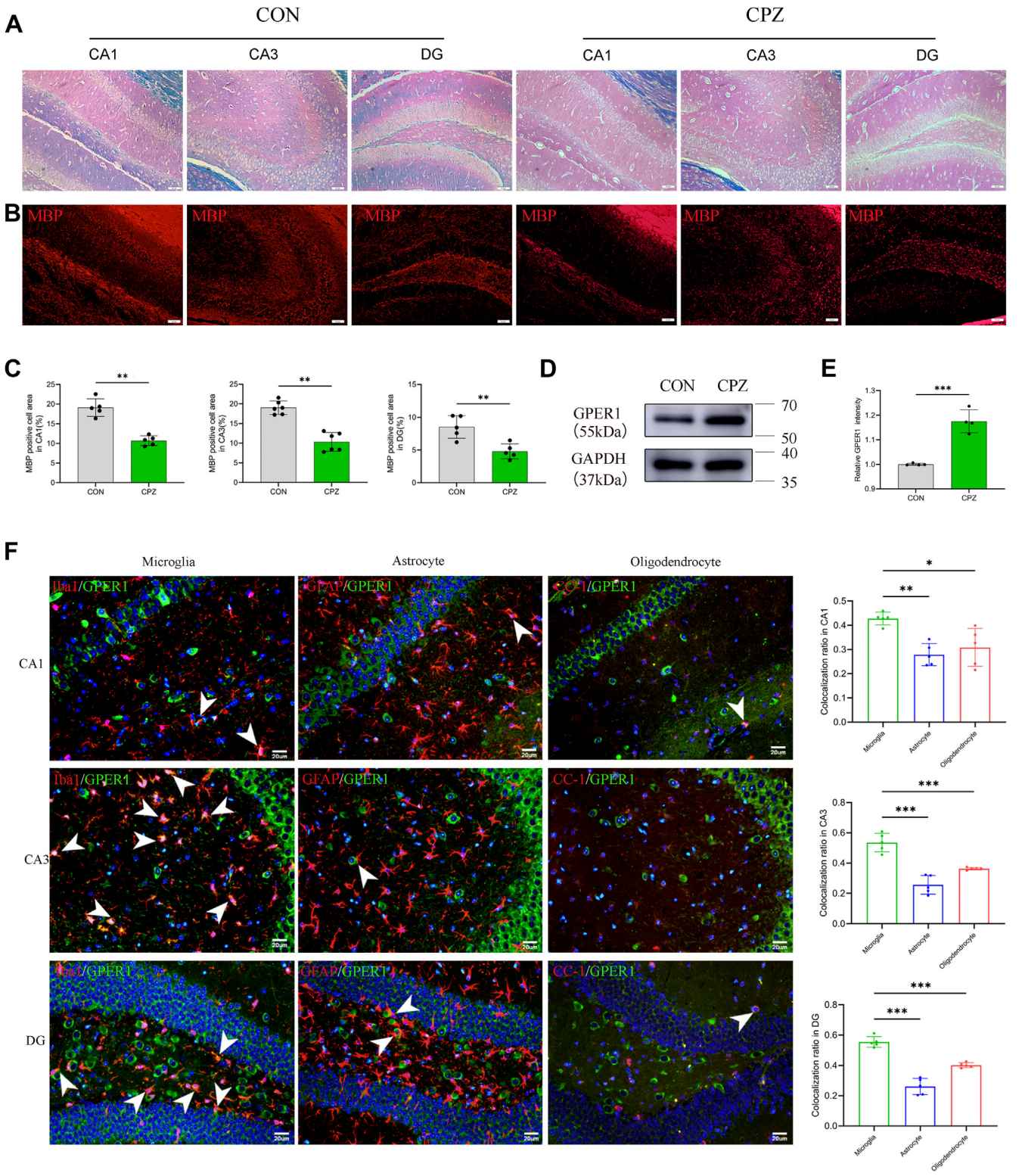

Figure 1. GPER1 is mainly expressed in microglia in the hippocampus of the cuprizone model. *A*, representative LFB images and quantification following cuprizone treatment (n = 5). Scale bar = 50 μm. *B*, *C*, representative MBP immunofluorescence images and quantification. Scale bar = 50 μm. *D*, *E*, representative Western blots bands and quantification of GPER1 in cuprizone mouse model (n = 4). *F*, colocalization of GPER1 (*green*) with Iba1, GFAP, and CC-1 (*red*) in the hippocampus of cuprizone-treated mice and the statistical analysis (n = 5). The co-labeled cells were marked with a *white arrow*. Scale bars = 20 μm. Statistical analysis was performed using two-tailed Student's *t*-tests and one-way ANOVA with Tukey's *post hoc* tests, and data were expressed as mean ± SD. *$p < 0.05$, **$p < 0.01$, ***$p < 0.001$. CPZ, cuprizone; DG, dentate gyrus; GPER1, G protein–coupled estrogen receptor; LFB, Luxol fast blue staining; MBP, myelin basic protein.

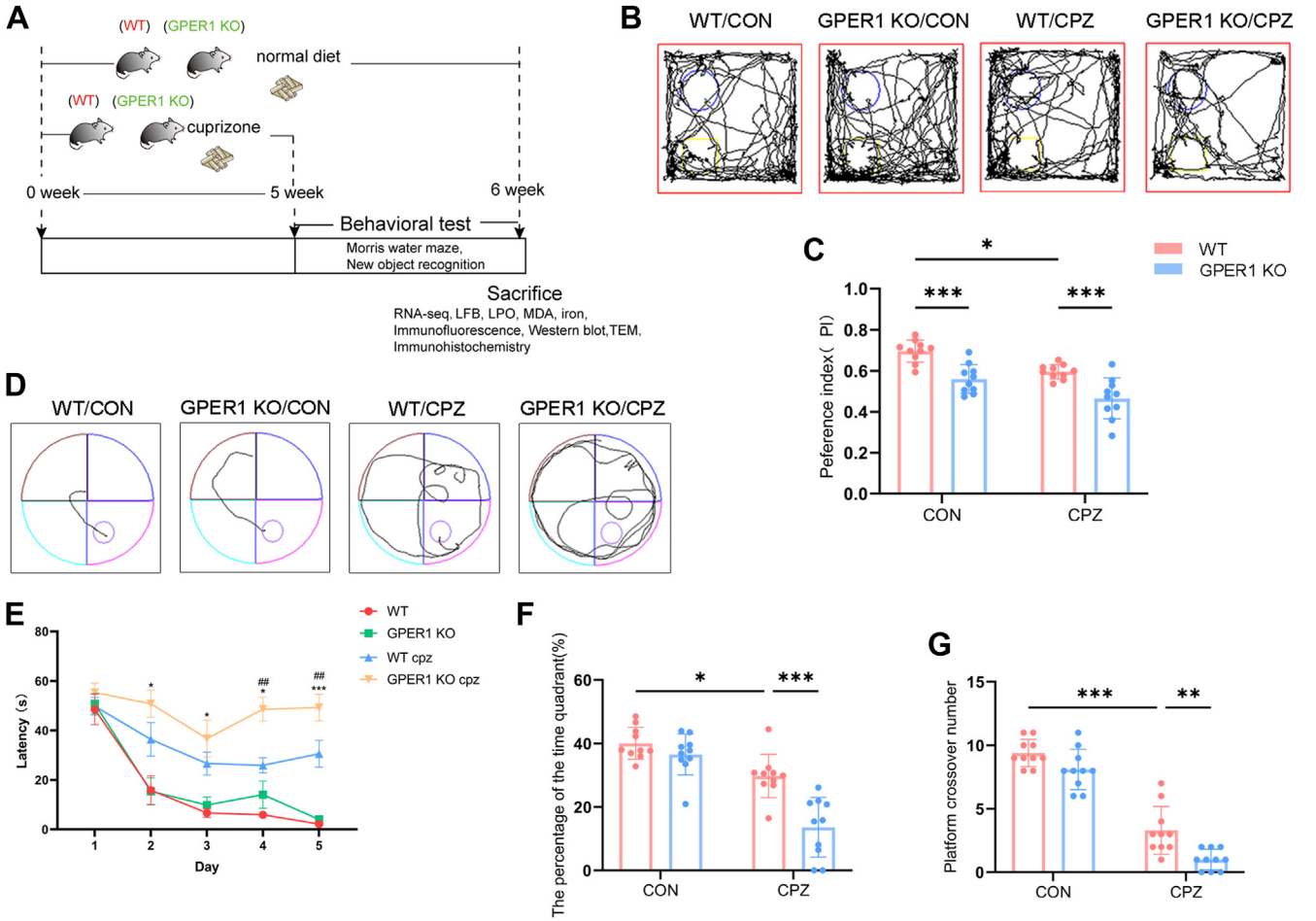

Figure 2. Effect of *GPER1* KO on memory cognition after demyelination. *A*, timeline diagram of cuprizone treatment and experimental analysis; *B*, *C*, new object recognition (NOR) and recognition index; *D*, representative positioning cruise track chart; *E–G*, quantification of escape latency, the percentage of time spent in the quadrant and platform crossing frequency; (n = 10). Statistics analyses were calculated using two-way ANOVA with Tukey's *post hoc* tests, and data were expressed as mean ± SD. $^{*}p < 0.05$, $^{**}p < 0.01$, $^{***}p < 0.001$. CPZ, cuprizone; GPER1, G protein–coupled estrogen receptor; KO, knockout; LFB, Luxol fast blue; LPO, lipid peroxidation; MDA, malondialdehyde; TEM, transmission electron microscopy.

(Fig. 5*D*). We then evaluated changes in ferroptosis markers. Results showed that *GPER1* KO promoted nuclear receptor coactivator 4 (NCOA4) expression but decreased the expression of TFR1 after myelin sheath injury, which explained the increase of iron ion in the hippocampus. Additionally, the expression of glutathione peroxidase 4 (GPX4) and XCT which are associated with lipid peroxide production (30), were decreased in *GPER1* KO mice with demyelinating, whereas NADPH oxidase 2 (NOX2) was increased. The expression of nuclear factor erythroid 2-related factor 2 (NRF2) and heme oxygenase (HO-1), which attenuate ferroptosis (31, 32), were decreased in *GPER1* KO/CPZ mice (Fig. 5, *E-L*). These *in vivo* data provide evidence that *GPER1* KO may promote ferroptosis after myelin damage.

GPER1 *KO reduced ferritin expression in microglia of the CPZ mouse model*

To investigate the effects of *GPER1* deletion on ferroptosis of microglia, we employed immunofluorescence colabeling method to detect the coexpression of Iba1 and ferritin in the hippocampus (33). Double-positive Iba1 and ferritin expression was only detected in the WT CPZ group (Fig. 6*A*). Consistent with the findings of Jhelum *et al.* (15), an increase in ferritin content and coexpression with microglia were observed in the WT mice of CPZ model. In contrast, ferritin levels were significantly reduced in the *GPER1* KO mice (Fig. 6, *B* and *C*). Previous studies reported a reduction of ferritin as a potential condition for ferroptosis occurrence (34). To further explore whether GPER1 influences microglial ferroptosis, we performed ultrastructural analysis using electron microscopy. The images showed activated microglia following CPZ treatment (Fig. 6*D*). In the WT/CPZ group, microglia displayed intact mitochondrial structures (*blue arrow*) with complete bilayer membrane cristae, whereas in the *GPER1* KO/CPZ group, increased mitochondrial membrane density and the disappearance of cristae were observed (Fig. 6*D*). These findings suggest that *GPER1* KO may induce ferroptosis of microglia.

GPER1 alleviated microglial ferroptosis

To further clarify the effects of GPER1 on microglia, the cultured microglia were subjected to a simulated

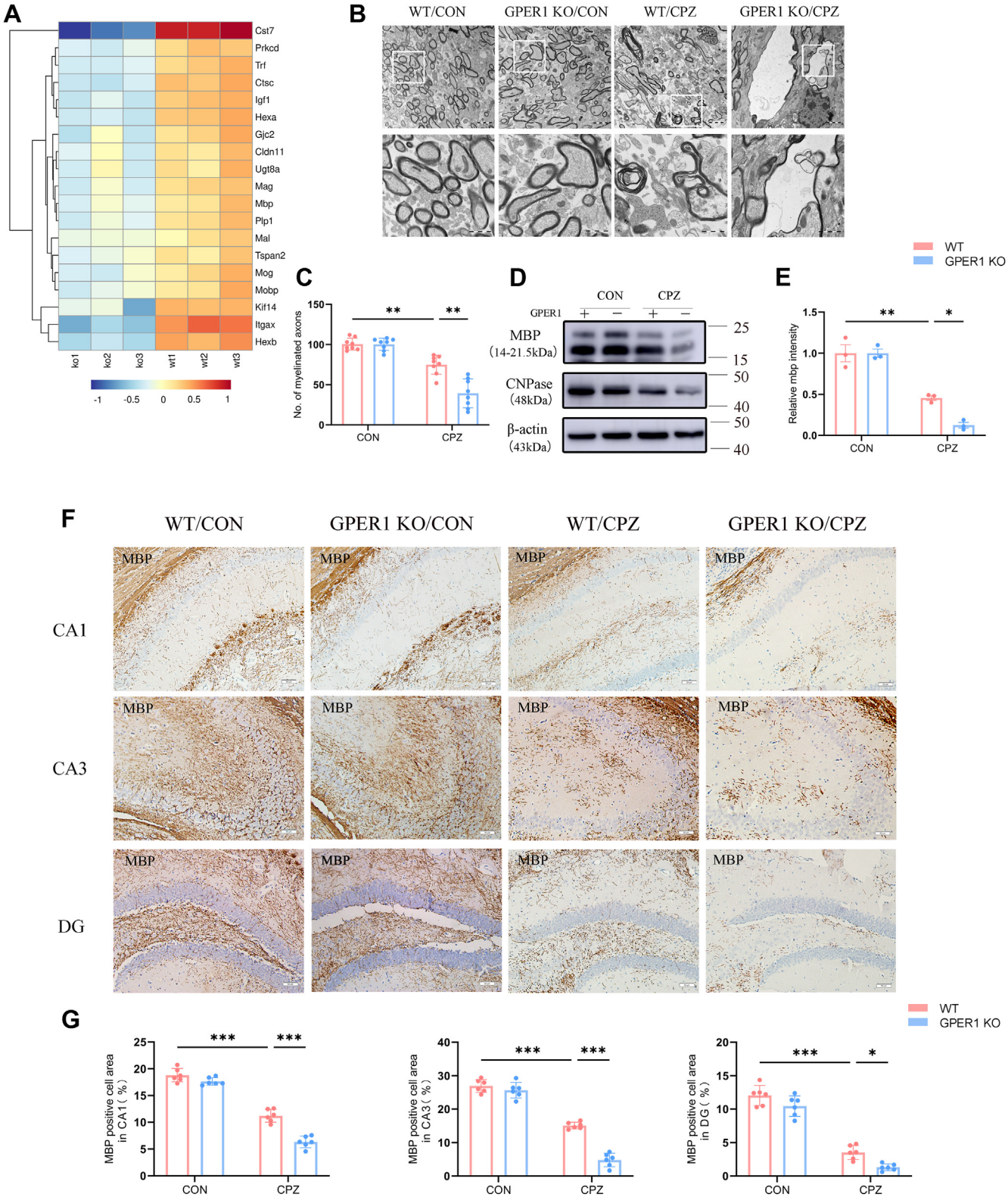

Figure 3. *GPER1* deficiency accelerates myelin damage in CPZ-treated mice. *A*, heatmaps showing downregulated genes involved in the formation of myelin, WT/CPZ mice *versus GPER1* KO/CPZ mice (n = 3). *B*, representative TEM images. *C*, the number of myelin-sheathed was calculated in each TEM image (n = 2, one image was taken from each of four sections in each animal). Scale bar = 2 μm (up), 1 μm (down). *D*, *E*, representative Western blot bands and quantification of MBP and CNPase in the hippocampus (n = 3). *F*, *G*, representative IHCs images and the statistical analysis of MBP in the hippocampus (n = 6). Scale bars = 50 μm. Statistics analyses were calculated using two-way ANOVA with Tukey's *post hoc* tests, and data were expressed as mean ± SD. *$p < 0.05$, **$p < 0.01$, ***$p < 0.001$. CPZ, cuprizone; GPER1, G protein–coupled estrogen receptor; KO, knockout; TEM, transmission electron microscopy.

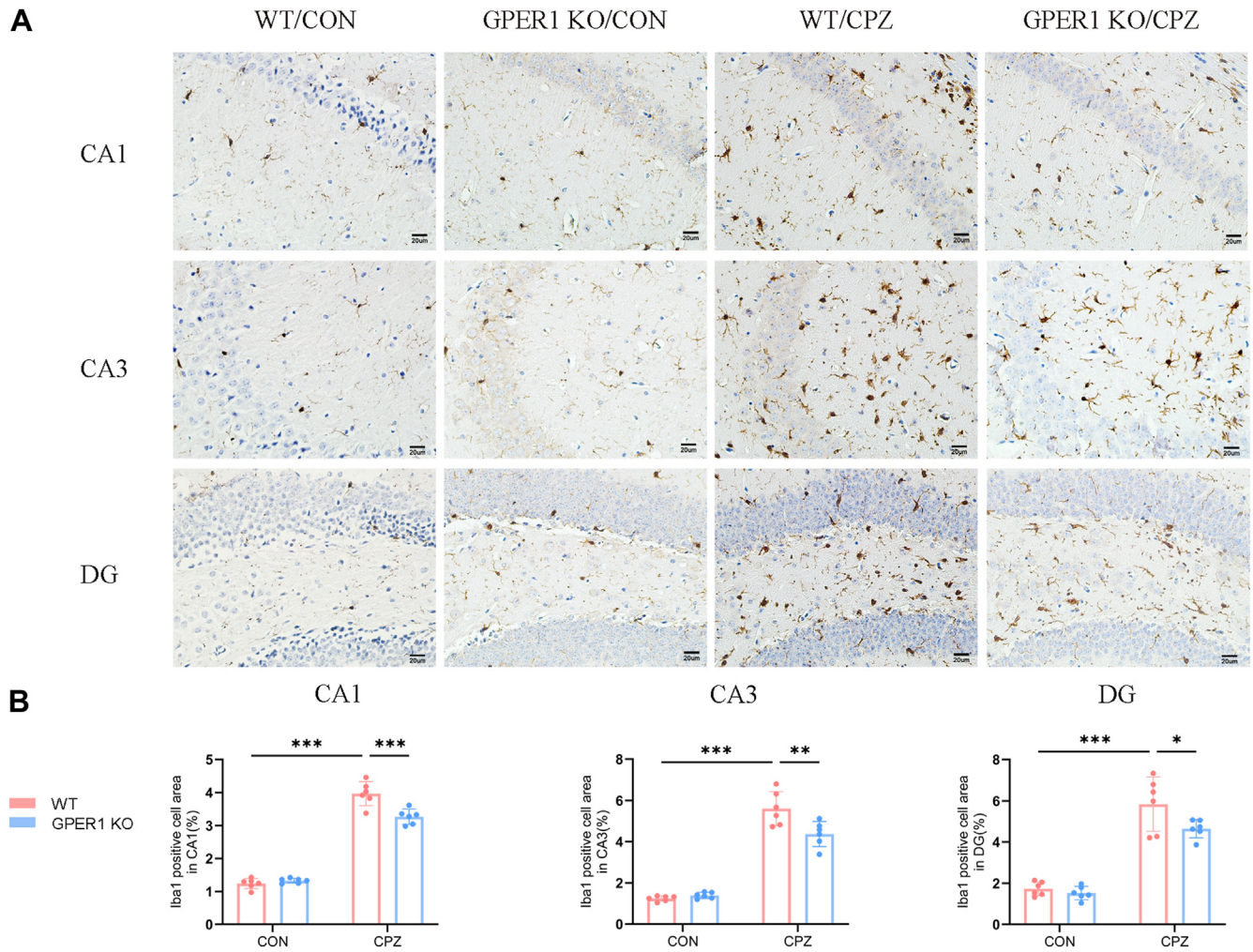

Figure 4. *GPER1* deficiency dramatically decreased microglia after demyelination. *A*, representative IHC staining image of Iba1 in the hippocampus (n = 6). Scale bars = 20 μm. *B*, the quantification of the proportion of the area occupied by Iba1. Statistical analyses were calculated using two-way ANOVA with Tukey's *post hoc* tests, and data are expressed as mean ± SD. *$p < 0.05$, **$p < 0.01$, ***$p < 0.001$. GPER1, G protein–coupled estrogen receptor 1; IHC, immunohistochemistry; KO, knockout.

demyelinating environment using extracted myelin sheath debris. The Western blot assay indicated a decrease in GPER1 expression following intervention by myelin debris (Fig. 7*B*). Perls' staining revealed that iron ion accumulation in the microglia after exposure to myelin debris was consistent with that observed following intervention with the ferroptosis inducer RSL3, which was in turn alleviated by treatment with G1, a GPER1 agonist (Fig. 7*C*). The dihydroethidium (DHE) staining results showed that myelin debris and RSL3 promoted the production of reactive oxygen species in the microglia, which was alleviated by G1 (Fig. 7, *D* and *E*). Furthermore, the myelin debris and RSL3 intervention reduced the mitochondrial membrane potential in microglia, which was also reversed by the G1 intervention (Fig. 7, *F* and *G*). Western blotting analysis demonstrated that after the myelin debris intervention, significantly reduced GPX4, XCT, and ferritin levels were observed, with further decreases occurring after treatment with G15, a GPER1 inhibitor. Conversely, the addition of G1 resulted in an upregulation of GPX4, XCT, and ferritin levels (Fig. 7, *H–K*).

GPER1 *KO reduced the phagocytic activity in the CPZ mouse model*

Next, transcriptomic profiling was carried out on the hippocampus of *GPER1* KO mice treated with CPZ as well as WT mice. The results indicated that the ferroptosis pathway was significantly enriched. Notably, pathways related to phagocytosis, like phagosome formation, and antigen presentation, showed significant differences (Fig. 8*A*). Moreover, the heatmap indicated the downregulation of factors related to phagocytosis, including positive regulators of the phagosome in the *GPER1* KO/CPZ group (*Ager, Trem2, and Fcgr1*) (Fig. 8*B*). Given the positive role of microglia in myelin debris clearance (9, 35), we speculate that *GPER1* KO induced ferroptosis of microglial cells may contribute to impaired microglial phagocytosis.

To further substantiate our conclusion regarding the impact of *GPER1* KO on microglial phagocytosis during CPZ-induced demyelination, we performed a colocalization analysis of MBP with Iba1 (*white arrow*). It was evident that microglia from *GPER1* KO mice exhibited significantly fewer colocalizations

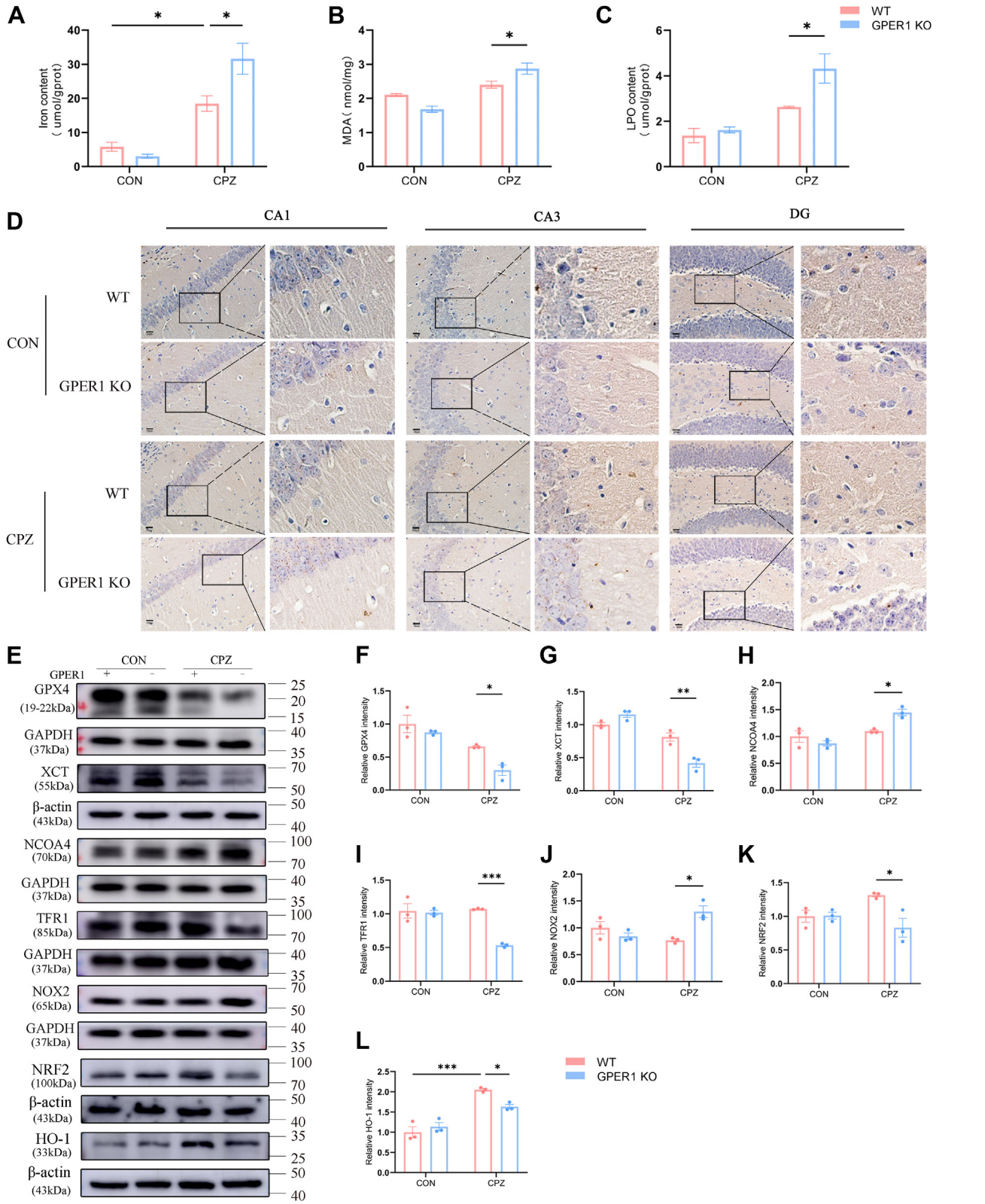

Figure 5. *GPER1* deficiency promotes ferroptosis after CPZ treatment. *A–C*, the concentration of iron, LPO, and MDA in brain tissues. *D*, representative images of Perls' staining in the hippocampus. Scale bar = 20 μm. *E–L*, representative Western blot images and statistical results of GPX4, XCT, NCOA4, TFR1, NOX2, NRF2, and HO-1 in the hippocampus (n = 3). Statistical analyses were conducted using two-way ANOVA with Tukey's *post hoc* tests. *$p < 0.05$, **$p < 0.01$, ***$p < 0.001$. CPZ, cuprizone; GPER1, G protein–coupled estrogen receptor 1; GPX4, glutathione peroxidase 4; HO-1, heme oxygenase; LPO, lipid peroxidation; MDA, malondialdehyde; NCOA4, nuclear receptor coactivator 4; NOX2, NADPH oxidase 2; NRF2, nuclear factor erythroid 2-related factor 2.

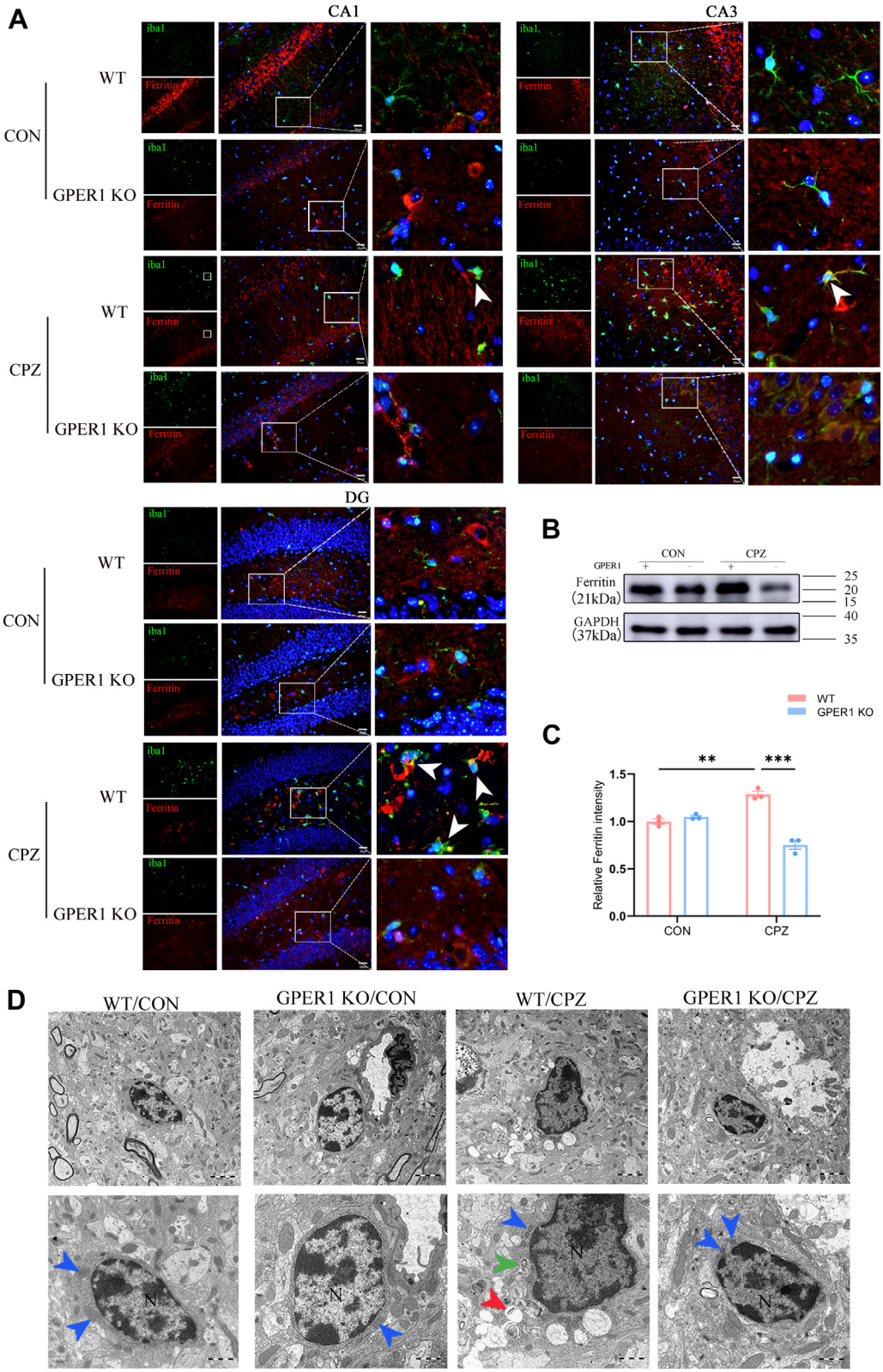

Figure 6. *GPER1* deficiency reduces the ferritin content in microglia after CPZ treatment. *A*, representative double immunohistochemical staining with Iba1 and ferritin image (n = 5). The co-labeled cells were marked with a *white arrow*. Scale bar = 20 μm. *B*, *C*, representative Western blot images and statistical results of ferritin (n = 3). Statistics analyses were calculated using two-way ANOVA with Tukey's *post hoc* tests, and data were expressed as mean ± SD. *$p < 0.05$, **$p < 0.01$, ***$p < 0.001$. *D*, representative electron microscopy images of microglia in the hippocampus. Mitochondria (*blue arrow*), intracellular vesicles (*red arrow*) and partially digested myelin products localized within the endosome (*green arrow*). Scale bars = 2 μm (up) and 1 μm (down). CPZ, cuprizone; GPER1, G protein–coupled estrogen receptor 1; KO, knockout.

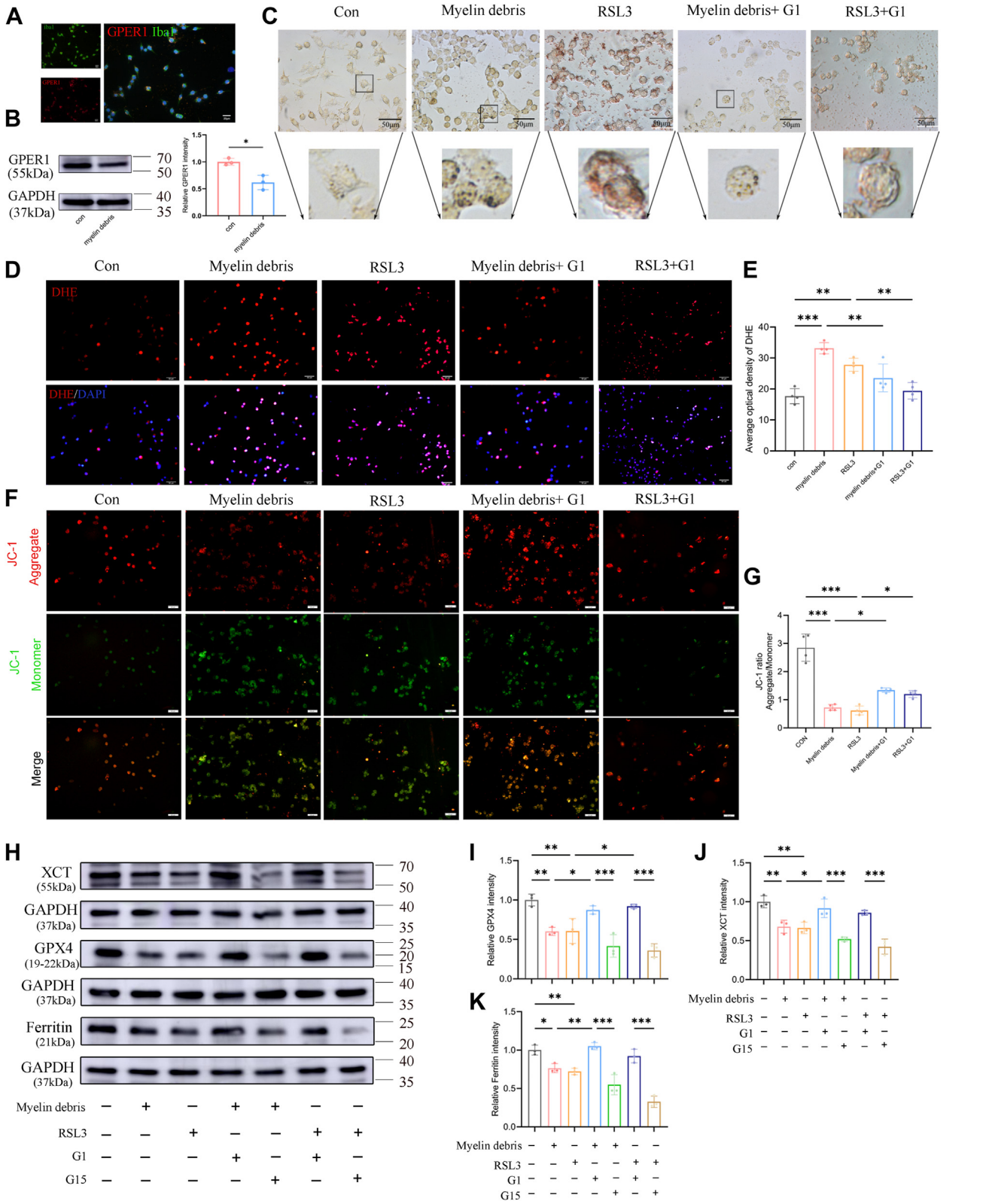

Figure 7. GPER1 affects ferroptosis in microglia. *A*, fluorescence images of GPER1 expression in microglia. Scale bar = 20 μm. *B*, representative Western blot images and statistical results of GPER1. Statistics were calculated using two-tailed Student's *t*-tests. *C*, distribution of iron localization in microglia after myelin debris intervention, bar = 50 μm. *D*, *E*, representative images of DHE labeling (*red*), and quantitation of DHE optical density, bar = 50 μm. *F*, *G*, representative immunofluorescence images and quantitation of JC-1 staining. *Red fluorescence* indicates JC-1 aggregates, and *green fluorescence* indicates monomeric JC-1. *H–K*, representative Western blot images and statistical results of GPX4, XCT, and ferritin in microglia (n = 3–4). Statistical analyses were calculated using one-way ANOVA with Tukey's *post hoc* tests, and data are expressed as mean ± SD. *$p < 0.05$, **$p < 0.01$, ***$p < 0.001$. DHE, dihydroethidium; GPER1, G protein–coupled estrogen receptor 1; GPX4, glutathione peroxidase 4.

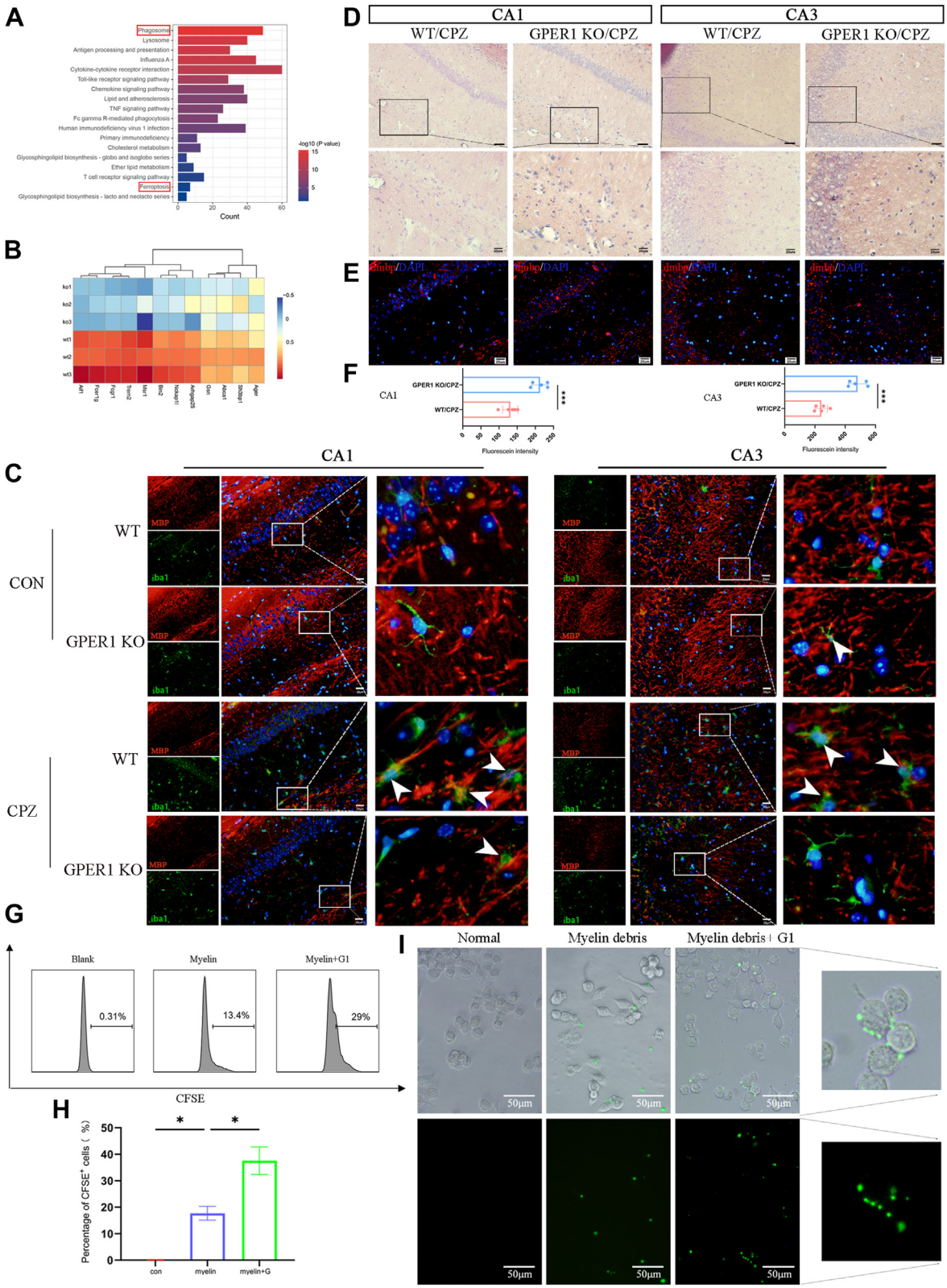

Figure 8. Deficiency of *GPER1* promotes the accumulation of myelin debris and weakened the function of microglial phagocytosis. *A*, bar graph illustrating the enriched pathways based on the differentially expressed genes in hippocampus from WT/CPZ mice *versus GPER1* KO/CPZ mice. *B*, heatmaps showing downregulated genes involved in phagocytosis in hippocampus. WT/CPZ mice *versus GPER1* KO/CPZ mice. *C*, double immunofluorescence staining for Iba1 and MBP in the hippocampus (n = 5). The co-labeled cells were marked with a *white arrow*. Scale bars = 20 μm. *D*, the image of Oil red O staining. Scale bars = 50 μm (up) and 20 μm (down). *E*, *F*, representative immunofluorescence and statistical results of degenerated myelin debris (dMBP) in hippocampus. Data were expressed as mean ± SD. Statistics were calculated using two-tailed Student's *t*-tests. ***$p < 0.001$. *G*, *H*, quantification of phagocytic CFSE-myelin debris by flow cytometry (n = 4–6). Statistical analyses were conducted using one-way ANOVA followed by Tukey's *post hoc* tests, and data were expressed as mean ± SD. *$p < 0.05$. *I*, phagocytic capacity of microglia after CFSE labeling of myelin fragments. Scale bar = 50 μm. CFSE, carboxyfluorescein succinimidyl ester; CPZ, cuprizone; GPER1, G protein–coupled estrogen receptor 1; KO, knockout; MBP, myelin basic protein.

of Mbp and Iba1 than did WT microglia in the demyelinating, suggesting impaired uptake of myelin debris by *GPER1* KO/CPZ mice (Fig. 8*C*). Furthermore, TEM images showed activated microglia (Fig. 6*D*). Higher magnification revealed cytoplasmic intracellular vesicles (*red arrow*) and products of myelin phagocytosis (*green arrow*) in WT/CPZ mice. However, intracellular vesicles and myelin fragments within the microglia were scarce in the *GPER1* KO/CPZ group (36–38). The phagocytic activity of microglia decreased in *GPER1* KO mice.

Impaired phagocytosis of microglia resulted in the accumulation of myelin debris. Myelin debris contained a substantial amount of lipid deposition, as detected by Oil Red O staining (29). Lipid deposition was evident in *GPER1* KO/CPZ mice (Fig. 8*D*). A specific marker for degraded myelin basic protein indicated increased myelin fragments in the *GPER1* KO/CPZ group (Fig. 8, *E* and *F*). Taken together, *GPER1* deficiency impaired the phagocytic activity of microglia.

BV2 cells were cultured and subjected to a simulated demyelinating environment using extracted myelin sheath debris. When carboxyfluorescein succinimidyl ester (CFSE)–labeled myelin debris was cocultured with microglia for 24 h, flow cytometry showed that G1 treatment significantly increased the microglial phagocytic rate (Fig. 8, *G* and *H*). Fluorescence microscopy revealed intracellular engulfment of myelin debris, as evidenced by green fluorescence. G1 treatment enhanced the intracellular green fluorescence (enlarged image) (Fig. 8*I*). Based on these results, we can conclude that GPER1 regulates microglial phagocytosis through ferroptosis and then affects the degree of myelin damage.

Discussion

In this study, CPZ-treated mice were used to investigate the effects of GPER1 in myelin damage by stimulating demyelination pathology. Since there is no sex difference in the distribution of GPER1 in the adult mouse brain, male mice were utilized as the study subjects to exclude the effect of the estrous cycle (39). We observed that the *GPER1* KO significantly increased the area of demyelination, decreased the express of OL, and aggravated the cognitive impairment of mice in CPZ model. Furthermore, we demonstrated that *GPER1* KO reduced the number of microglia through including ferroptosis, which resulted in inefficient clearance and degradation of myelin debris. These results demonstrated that GPER1 may be a new target for myelin repair.

Demyelination of the CNS can impair the transmission of nerve impulses, resulting in neurological damage and degeneration, which ultimately leads to neurological abnormalities. Patients with central demyelination often have spatial learning and memory disorders, which seriously affect the prognosis of the disease. The hippocampus is a crucial brain region for regulating learning and memory (40). Therefore, it is crucial to illustrate the molecular mechanisms regulating hippocampal demyelination to mitigate cognitive impairment. The novel estrogen receptor GPER1 is widely distributed in various brain regions and mediates the neuroprotective effect of estrogen. Previous studies have shown that GPER1 expression negatively correlates with myelin injuries in the corpus callosum of rats (41). However, we found an upregulation of GPER1 in the hippocampus of the CPZ model. Meanwhile, downregulation of GPER1 was obversed in microglia directly treated with myelin debris. Due to the differences in the degree and mechanism of myelin damage in the white matter and gray matter (42, 43), we hypothesized that the increase in GPER1 expression may be an adaptive response to the pathological condition of myelin damage in the hippocampus. Activating GPER1 has been reported to enhance spatial recognition memory in ovariectomized rats (44, 45) and episodic recognition memory in AD mice (24). Conversely, inhibition of GPER1 expression aggravated neural damage and cognitive impairment (46) Studies have shown that GPER1 agonists effectively promoted remyelination and increased the expression of mature OLs in the rat CPZ model. Consistent with these results, this study showed that *GPER1* KO with severe myelin damage further reduced the ability of spatial learning and episodic memory in myelin-damaged mice. In addition, we observed further reduction for the content of OPCs and OLs in *GPER1* KO mice, which illustrated the reason of remyelination disorder.

We found that in addition to its expression in OLs (47), GPER1 was also highly expressed in microglia after myelin injury. Microglia, the primary innate immune cells in the CNS, can relieve tissue damaged by phagocytosing cell debris (48). Impaired microglial phagocytosis may lead to insufficient clearance of myelin debris, thereby delaying or hindering remyelination (49). Studies have shown the significant activation of microglia in the hippocampus after myelin damage (50). Consistent with these reports, we found that the activation of a large proportion of microglia in the hippocampus of mice with myelin injury. Interestingly, microglia numbers decreased in *GPER1* KO mice. Moreover, deficiency of *GPER1* in mice decreased phagocytic activity and impaired ability to clear myelin debris. However, the regulating mechanism of GPER1 on myelin debris clearance remains unclear.

Accumulation of myelin debris in microglia was found to promote susceptibility to microglial ferroptosis (17), and the iron-overloaded microglia can reduce their phagocytic capacity (21). Ferroptosis is a mode of cell death characterized by accumulation of lipid peroxides and iron overload. Microglia, being iron-rich cells in the nervous system, are particularly susceptible to ferroptosis (51, 52). Recent studies have shown that GPER1 inhibits ferroptosis by mediating NRF2/GPX4 signaling after cerebral ischemia-reperfusion injury (27). However, the effect of GPER1 on ferroptosis in microglia remains to be elucidated. In the present study, we found a significant increase in free iron and lipid peroxides in the hippocampus of *GPER1* KO mice with damaged myelin. Meanwhile, the expression of ferroptosis-related proteins such as NOX2, which is involved in lipid peroxide production, was increased, while the levels of XCT, GPX4, NRF2, and HO-1, which are involved in antioxidation, were decreased. NCOA4 is a cargo receptor that binds to ferritin heavy chains and transports them to autophagosomes for degradation

(phagocytoferrin) (48). Whereas ferritin degradation increases susceptibility to ferroptosis by releasing biologically active iron into the cytoplasm (15, 51). Of note, GPER1 regulates ferritin expression in microglia (53). In our study, *GPER1* KO mice showed increased NCOA4 expression and decreased ferritin content. Furthermore, *GPER1* KO mice showed loss of mitochondrial cristae in microglia, which reflected ferroptosis in microglia. To compensate for the untargeted study of microglia using global KO mice in the *in vivo* experiments, we further demonstrated, *in vitro* using the microglial cell line BV-2, that GPER1 inhibited microglial ferroptosis induced by myelin debris.

It should be noted that this study has some limitations. First, the *in vivo* experiments did not use *GPER1* cKO mice for the targeted regulation of microglia. Second, considering the regional differences in GPER1 expression and varying degrees of myelin damage varies in different brain regions, subsequent studies should explore the role of GPER1 on myelin damage in other brain regions. Finally, our experiments confirmed the function of GPER1 in regulating demyelination through microglia iron death, but whether GPER1 mediates the effect of other cellular iron death on myelin repair requires further investigation.

In conclusion, this study identifies a potential mechanism of GPER1 involvement in demyelination. Ferroptosis of microglial cells caused by the deletion of *GPER1* leads to the inability to phagocyte large amounts of myelin debris. The accumulation of myelin debris reduces OLs and hinders myelin repair, which in turn aggravates myelin damage and causes cognitive dysfunction (Fig. 9).

Experimental procedures

Animals

Professor Rong Wei Fang of Shanghai Jiao Tong University provided the breeding pairs of mice with *GPER1* KO mice were generated by deleting 17 nucleotides of GPER1 using the CRISPR-CAS9 system (54). We obtained approval to use WT animals from Ningxia Medical University in Yin Chuan, China. All offspring were genotyped. To ensure their welfare, all mice were housed in a pathogen-free facility with access to sterilized water and ad libitum access to food. The animal protocols followed the guidelines of the National Research Council's Guide for the Care and Use of Laboratory Animals and were approved by the Animal Care Committee of Ningxia Medical University (Approval No: 2020–317; approval date April 3, 2020).

Six-week-old male WT and *GPER1* KO mice were assigned to experimental or control groups. Experimental groups (WT/CPZ and *GPER1* KO/CPZ) were fed a diet containing 0.2% CPZ (SIGMA, C9012) for 5 weeks to induce demyelination. Control groups (WT/CON and *GPER1* KO/CON (n = 18 per group) were fed a normal diet for the same duration. Following the dietary treatment, behavioral trainings were performed, and all the mice were returned to normal diet. After completing the behavioral test, all the mice were euthanized.

Ten C57BL/6J male mice aged 12 weeks of age were used to extract myelin debris.

Behavioral test

A series of behavioral procedures were used to assess the main dysfunctions of mice in the experiment group (n = 10).

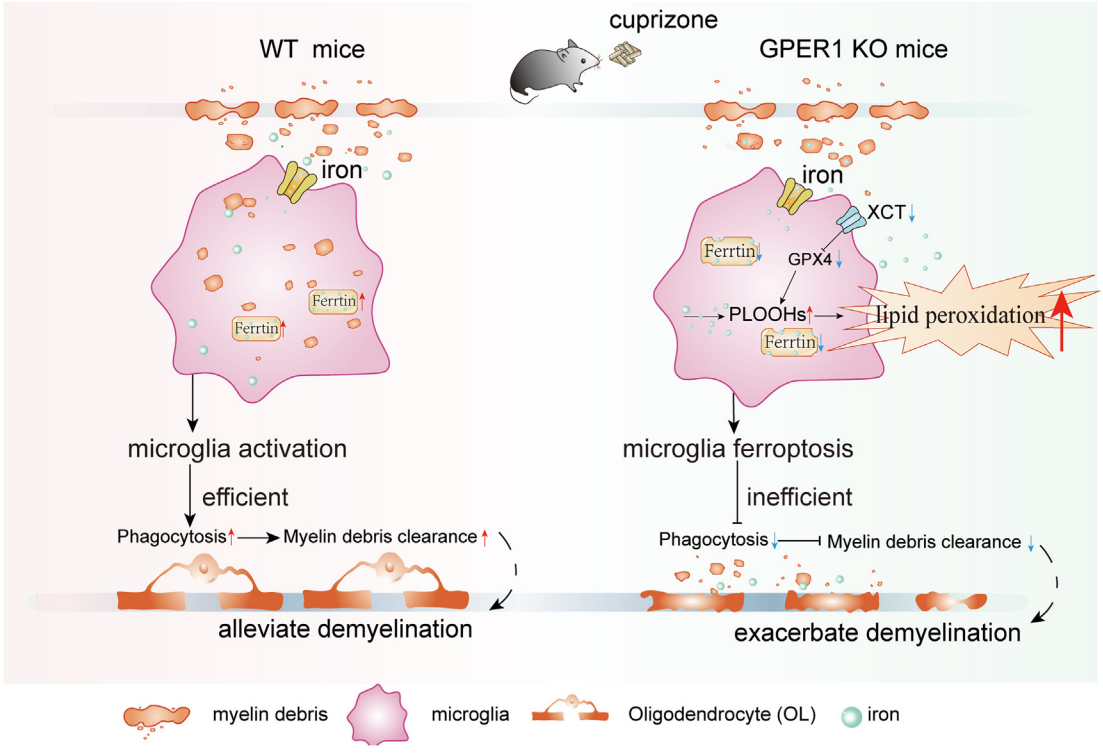

Figure 9. Graphical abstract. *GPER1* KO leads to microglia ferroptosis in CPZ model. The subsequent reduction of microglia leads to impaired phagocytosis and massive accumulation of myelin debris, which exacerbates myelin damage. CPZ, cuprizone; GPER1, G protein–coupled estrogen receptor 1; GPX4, glutathione peroxidase 4; KO, knockout.

All mice were allowed to acclimate to the environment for 24 h. The experiments were proceeded between 6:30 AM and 11:30 AM. A digital camera and software (smart 3.0) were used to record the general locomotor activity of the mice.

New object recognition

The NOR is an experiment used to assesses the learning and cognitive abilities of experimental animals by measuring their preference for new and familiar objects. In this experiment, mice were acclimated in an open field for 10 min. Following acclimation, an identical object was placed in the field, and each mouse was given 10 min to explore it. On the following day, one of the objects was replaced with a new one, and the mouse was again allowed to explore for 10 min. The duration of exploration for both the previous and new objects was carefully recorded. The identification index was recorded as follows: (time novel)/(time novel + time old).

Morris water maze

The MWM is a traditional tool used to evaluate the memory and learning capabilities of mice. In this study, an experimental configuration was established, comprising a pool of circular shapes. The pool had dimensions of a radius measuring 40 cm and a depth of 30 cm. The pool was divided into four quadrants, with a 10 cm-wide platform placed in the second quadrant. To ensure consistency, the water in the pool, which contained white dye, was consistently maintained 1 cm above the platform' surface. The temperature of the water was maintained stable at 22 ± 2 °C. Distinct visual markers in the shapes of a circle, triangle, square, and cross were attached at strategic points around the pool. The training phase lasted for a total of 6 days. During the first 5 days, each mouse was placed in the water maze for 60 s in each quadrant to locate the hidden platform. The experiment ended once the mouse successfully found the platform. On the sixth day, the platform was removed. The time required for mice to discover the location of the original platform (referred to as the latency time), the percentage of time in the platform quadrant, and the frequency of crossing the location of the original platform were recorded for subsequent analysis.

Luxol fast blue staining

The Luxol fast blue staining kit was purchased and used to evaluate histological changes associated with myelin loss. The brain sections were dewaxed using 95% ethanol and immersed in the Luxol fast blue solution at 37 °C for 12 h. On the following day, each section was placed in 95% alcohol for 1 s and rinsed with water. The differentiation solution was then dropped onto the sections for 15 s. Subsequently, the sections were stained with eosin dye for 2 min, dehydrated, and sealed. Images were captured using an Olympus BX51 microscope (Olympus).

RNA-sequencing analyses

Both WT and GPER1 KO mice were subjected to the CPZ regimen, with three biological replicates per group. Half of the mouse hippocampus from each sample was extracted for RNA isolation, and the remaining tissues were used for TEM analysis. PolyA mRNA enrichment was performed using oligo(dT) magnetic beads, and the RNA was fragmented into approximately 300-bp fragments. The fragmented RNA was then used to construct fragments for the cDNA library. Library quality was evaluated using a Bioanalyzer (Agilent 2100). Paired-end sequencing of these libraries was conducted on the Illumina HiSeq platform employing next-generation sequencing technology. DESeq was used for differential gene expression analysis applying the following criteria: $p < 0.05$; $|\log FC| > 1$. A differential gene expression heat map was created using the pheatmap software package. The data have been submitted to the Gene Expression Omnibus database of the National Center for Biotechnology Information (ID: PRJNA1021276).

Immunohistochemistry staining

Brain sections were routinely deparaffinized, rehydrated, and subjected to antigen retrieval by boiling in citrate solution for 17 min. After cooling to room temperature, the sections were treated with a peroxidase blocker and incubated for 20 min. The primary antibodies used were as follows: Iba1 (1:5000, ab178847, Abcam), MBP (1:500, ab218011, Abcam), and CNPase (1:200, ab6319, Abcam). The following day, after washing off the primary antibody, the sections were incubated with a reaction enhancer for 20 min. Subsequently, a secondary antibody was incubated for 1 h at 37 °C. A diaminobenzidine solution was then used for the color reaction, and nuclei were stained with hematoxylin. Sections were routinely dehydrated and sealed. Microscopic visualization of the result was performed using (Olympus, BX51 microscope). Positive staining was observed in the hippocampal CA1, CA3, and dentate gyrus regions. Statistical analysis of the staining was conducted using Image J software.

Oil red O staining

Frozen slices (15 μm) were brought to room temperature and stained using an Oli Red O kit (Solarbio). Subsequently, the reaction solution was added dropwise to each section. Finally, the nuclei were stained with hematoxylin, and the slides were sealed with glycerin gelatin. The images were captured using an Olympus microscope.

Transmission electron microscopy

The hippocampus was isolated under the stereomicroscope, with each block measuring about a cubic millimeter. Following established protocols, brain tissues were initially immersed in 2.5% glutaraldehyde (55). The tissues were then fixed with osmic acid. After dewatering with an alcohol gradient, the tissues were embedded in resin. Samples were processed for semithin slices. Finally, the ultrastructure was observed *via* electron microscopy (transmission electron microscope, HITACHI).

Measurement of the contents of MDA, iron, and LPO levels

MDA assay kits were obtained from Solarbio. Tissue specimens were lysed for protein extraction, the working solution was added three times, and the protein concentration was

measured. A 100 °C water bath was used to heat the preparation for 60 min. Afterward, it was cooled down and subsequently centrifuged at 8000×*g* for 10 min. The supernatant was collected, and the absorbance values were measured at 450, 532, and 600 nm using a microplate spectrophotometer (Thermo Fisher Scientific).

Iron ion colorimetric detection and LPO assay kits were acquired from Nanjing Jiancheng. All tissues were weighed, and a homogenate was prepared by adding nine times their volume of normal saline. Protein concentration was determined according to manufacturer's guidelines. For the iron ion assay, each sample was heated in a boiling water bath for 5 min. Subsequently, the supernatant was transferred to a 96-well plate to measure absorbance at 520 nm. The LPO levels were also measured based on the manufacturer's guidelines. Each sample was heated in a 45 °C water bath for 60 min, after which the supernatant was added to a 96-well plate. Absorbance was gauged at 586 nm. The absorbance values were detected using a Thermo Fisher Scientific microplate spectrophotometer.

Cell culture and treatment

The BV2 mouse microglia cell line (Procell, CL0493 A) was cultured in Dulbecco's modified Eagle medium (Gibco) supplemented with 10% fetal bovine serum and 1% penicillin-streptomycin solution. The cells were grown at 37 °C in a humidified environment with 5% CO_2. The cell groups were as follows: control, myelin debris (35 ug/ml), RSL3 (1.5 μM) (ferroptosis agonist), myelin debris + G1(1.5 μM) (myelin debris with addition of the GPER1 agonist G1), myelin + G15 (1 μM) (myelin debris group with addition of the GPER1 inhibitor G15), and RSL3+G1, RSL3+G15. Cells were pretreated with G1 and G15 for 2 h and then stimulated with myelin debris and RSL3 for 24 h, respectively.

Myelin debris preparation and fluorescent labeling

Mice were euthanized using a 3.5% isoflurane mixture (N2O:O2 = 70:30) and then immersed in alcohol for 30 min. The brains were extracted and placed in a 0.32 M sucrose solution. The tissue was ground in a submerged homogenizer, and then 0.83 M sucrose was gradually added to create a stratified solution. High-speed ultracentrifugation (Thermo Fisher, MTX150) at 100,000 rpm and 4 °C for 45 min was used to isolate crude myelin debris between the solution layers. The crude myelin debris was resuspended in Tris-HCL buffer, homogenized for 60 s, and centrifuged again for 45 min under the same conditions. The myelin sheaths were weighed, resuspended in sterile phosphate-buffered saline (PBS), and centrifuged at 12,000 rpm for 10 min. The supernatant was discarded, and an appropriate amount of PBS was added to achieve a myelin debris concentration of 100 mg/ml. Myelin debris was labeled with 50 μM CFSE for 30 min at 37 °C in the dark and stored at −80 °C.

Perls' staining

Using the diaminobenzidine-enhanced Perls' staining kit (Solarbio), we identified the deposition of iron-containing in brain tissue. The tissue sections were deparaffinized, and cell slides were fixed in paraformaldehyde. Both the tissue sections and cell slides were treated with Perls' working solution for 30 min, following the manufacturer's instructions. Subsequently, incubation with enhancement solutions was applied sequentially. After dehydration, the slices were sealed with neutral gum. The staining results were captured using a microscope (Olympus, BX51).

Flow cytometry

Flow cytometry was used to assess the phagocytic capacity of microglia. BV2-microglia (12×10^6) were cultured in 6-well plates. CFSE-labeled myelin debris (35 μg/ml) and G1(1.5 μm) were added and incubated for 24 h at 37 °C with 5% CO_2. Following incubation, excess myelin debris was washed away with PBS. The cells were harvested and analyzed using Cyto FLEX flow cytometer (Beckman Coulter).

DHE staining

DHE staining (S0063, Beyotime) was performed to evaluate the accumulation of reactive oxygen species. BV2 cells were seeded at a density of 2×10^4 cells/well in 24-well culture plates plated with cell-climbing slices. Subsequently, different concentrations of myelin debris, G1, and RSL3 were added. After a 24-h incubation, each well was incubated with 1 μM DHE reagent for 30 min and then rinsed with PBS three times after incubation. The nuclei of the cells were then stained with 4–6-diamidino-2-phenylindole at room temperature. Subsequently, the slices were observed under an Olympus fluorescent microscope. Quantitative analysis was performed using Image J software.

Mitochondrial membrane potential assay

JC-1 fluorescent dye (KGA603, KeyGEN BioTECH) was used to detect the mitochondrial membrane potential. Briefly, cells were seeded in a 24-well plate and incubated overnight. Following treatment, the cells were stained with the JC-1 solution for 30 min. Finally, results were captured using the Olympus fluorescent microscope.

Western blot

Animals in each group were deeply anesthetized with isoflurane. Hippocampal tissues and cells were homogenized. After acquiring the supernatant, the bicinchoninic acid assay kit was employed to ascertain the protein concentrations (KEYGEN). The separation of proteins was conducted by employing 10% and 12% SDS-PAGE gels, followed by the transfer of the proteins to polyvinylidene fluoride membranes. Then a solution of 10% skim milk was applied for 1 h. The primary antibodies were utilized as follows: GPER1(1:1000 dilution, ab39742, Abcam), MBP (1:1000 dilution, ab218011, Abcam), CNPase (1:1000, ab6319, Abcam), GPX4 (1:1000, ab125066, Abcam), XCT (1:1000, ab216876, Abcam), Ferritin (1:1000, ab75973, Abcam), TFR1 (1:1000, A5865, Abclonal), NCOA4(1:1000, A25307, Abclonal), NOX2(1:1000, A19701, Abclonal), NRF2(1:1000, E5F1A, Cell Signaling Technology),

and HO-1(1:1000, ab68477, Abcam). The next day, secondary antibodies (goat anti-mouse and goat anti-rabbit, 1:5,000, Santa Cruz Biotechnology) were added to the membranes for 1 hour, followed by an additional wash. Protein bands were visualized using enhanced chemiluminescence luminous (Thermo Scientific, NO. 32106) and scanned by Amersham Imager600 (GE).

Immunofluorescence staining

Paraffin-embedded sections from each group were dewaxed and rehydrated. The antigen in the section was then repaired with a boiled citric acid solution. A sealer of 1% BSA, 1% NGs, and 0.3% Triton X-100 was configured and added dropwise to the sections and incubated at 37 °C for 1 h. The cells were fixed in paraformaldehyde for 30 min. Cell membranes were lysed with 0.3% TritonX-100, and the cells were then incubated with serum for 1 h. Subsequently, the slices and cells were incubated with primary antibodies at 4 °C overnight. The antibodies were utilized: GPER1 (1:200, ab39742, Abcam), Iba1 (1:800, ab283319, Abcam), NG2 (1:200, ab275024, Abcam), MBP (1:500, ab218011, Abcam), degraded myelin basic protein (1:1000, AB5864, Millipore), and ferritin (1:200, ab75973, Abcam). After PBS washed, samples were incubated with fluorescent secondary antibodies for 2 h in the dark. Images were captured using an Olympus fluorescence microscope.

Statistical analyses

All experiments were conducted at least three times. Data were analyzed using Prism software version 8 (GraphPad Software). Two-tailed Student's t-tests and one-way ANOVA were used to assess differences between two or more groups. Two-way ANOVA was applied for datasets with two factors: mouse genotype and diet. Tukey's *post hoc* test was used for pairwise comparisons between groups. Results are presented as mean ± standard deviation (SD). p value < 0.05 was set as the threshold for statistical significance.

Data availability

The RNA-seq data have been submitted to the National Center for Biotechnology Information's Gene Expression Omnibus database (ID: PRJNA1021276). https://www.ncbi.nlm.nih.gov/Traces/study/?acc=PRJNA1021276&o=acc_s%3Aa.

Supporting information—This article contains supporting information.

Acknowledgments—We are grateful to Professor Weifang Rong of Shanghai Jiao Tong University for providing GPER1 KO mice.

Author contributions—Y. L., Z. F., X. M., J. L., C. Z., and Y. S. writing–review & editing; Y. L., Z. F., and J. L. software; Y. L., Z. F., X. M., J. L., C. Z., H. L., Z. Y., and T. W. methodology; Y. L., Z. F., X. M., and J. L. data curation; X. M. writing–original draft; X. M. and J. Li. conceptualization; Y. S. and J. Li. funding acquisition. J. Li. visualization; J. Li. validation; J. Li. supervision; J. Li. project administration.

Funding and additional information—This work was supported by the National Natural Science Foundation of China [grant number 82060238]; the Ningxia Natural Science Foundation, China [grant number 2022AAC02026]; and the Ningxia Key Research and Development Project [grant number 2021BEB04042]. The animal study protocol was approved by the Medical Ethics Review Committee of Ningxia Medical University (approval no.2020–317; approval date April 3, 2020).

Conflicts of interest—The authors declare that they have no conflicts of interest with the contents of this article.

Abbreviations—The abbreviations used are: CA, cornu ammonis; CFSE, carboxyfluorescein succinimidyl ester; CNS, central nervous system; CPZ, cuprizone; DHE, dihydroethidium; GPER1, G protein–coupled estrogen receptor; GPX4, glutathione peroxidase 4; HO-1, heme oxygenase; IHC, immunohistochemistry; KO, knockout; LFB, Luxol fast blue staining; LPO, lipid peroxidation; MBP, myelin basic protein; MDA, malondialdehyde; MWM, Morris water maze; NCOA4, nuclear receptor coactivator 4; NOR, new object recognition; NOX2, NADPH oxidase 2; NRF2, nuclear factor erythroid 2-related factor 2; OPCs, oligodendrocyte precursor cells; TEM, transmission electron microscopy; WT, wild type.

References

1. Rocca, M. A., Barkhof, F., De Luca, J., Frisén, J., Geurts, J. J. G., Hulst, H. E., *et al.* (2018) The hippocampus in multiple sclerosis. *Lancet Neurol.* **17**, 918–926
2. Katsel, P., Davis, K., and Haroutunian, V. (2005) Variations in myelin and oligodendrocyte-related gene expression across multiple brain regions in schizophrenia: a gene ontology study. *Schizophr. Res.* **79**, 157–173
3. Luo, X., Li, K., Zeng, Q., Huang, P., Jiaerken, Y., Wang, S., *et al.* (2019) Application of T1-/T2-weighted ratio mapping to elucidate intracortical demyelination process in the Alzheimer's disease continuum. *Front. Neurosci.* **13**, 904
4. Mathys, H., Davila-Velderrain, J., Peng, Z., Gao, F., Mohammadi, S., Young, J. Z., *et al.* (2019) Single-cell transcriptomic analysis of Alzheimer's disease. *Nature* **570**, 332–337
5. Zhu, X., Yao, Y., Hu, Y., Yang, J., Zhang, C., He, Y., *et al.* (2021) Valproic acid suppresses cuprizone-induced hippocampal demyelination and anxiety-like behavior by promoting cholesterol biosynthesis. *Neurobiol. Dis.* **158**, 105489
6. Wegrzyn, D., Juckel, G., and Faissner, A. (2022) Structural and functional deviations of the Hippocampus in schizophrenia and schizophrenia animal models. *Int. J. Mol. Sci.* **23**, 5482
7. Chen, J. F., Liu, K., Hu, B., Li, R. R., Xin, W., Chen, H., *et al.* (2021) Enhancing myelin renewal reverses cognitive dysfunction in a murine model of Alzheimer's disease. *Neuron* **109**, 2292–2307.e2295
8. Kotter, M. R., Li, W. W., Zhao, C., and Franklin, R. J. (2006) Myelin impairs CNS remyelination by inhibiting oligodendrocyte precursor cell differentiation. *J. Neurosci.* **26**, 328–332
9. Qin, C., Chu, Y., Zhou, L., Dong, M., Wang, W., and Tian, D. (2023) Haste makes waste: staged suppression of autophagic-lysosomal pathway in microglia promotes the efficient clearance of myelin debris. *Autophagy* **19**, 1896–1898
10. Li, C., Wang, Y., Xing, Y., Han, J., Zhang, Y., Zhang, A., *et al.* (2022) Regulation of microglia phagocytosis and potential involvement of exercise. *Front. Cell. Neurosci.* **16**, 953534
11. McNamara, N. B., Munro, D. A. D., Bestard-Cuche, N., Uyeda, A., Bogie, J. F. J., Hoffmann, A., *et al.* (2023) Microglia regulate central nervous system myelin growth and integrity. *Nature* **613**, 120–129
12. Ren, J., Dai, C., Zhou, X., Barnes, J., Chen, X., Wang, Y., *et al.* (2021) Qki is an essential regulator of microglial phagocytosis in demyelination. *J. Exp. Med.* **218**, e20190348

13. Wies Mancini, V., Di Pietro, A., and Pasquini, L. (2023) Microglia depletion as a therapeutic strategy: friend or foe in multiple sclerosis models? *Neural. Regen Res.* **18**, 267–272
14. Dixon, S., Lemberg, K., Lamprecht, M., Skouta, R., Zaitsev, E., Gleason, C., *et al.* (2012) Ferroptosis: an iron-dependent form of nonapoptotic cell death. *Cell* **149**, 1060–1072
15. Jhelum, P., Santos-Nogueira, E., Teo, W., Haumont, A., Lenoël, I., Stys, P., *et al.* (2020) Ferroptosis mediates cuprizone-induced loss of oligodendrocytes and demyelination. *J. Neurosci.* **40**, 9327–9341
16. Andersen, H. H., Johnsen, K. B., and Moos, T. (2014) Iron deposits in the chronically inflamed central nervous system and contributes to neurodegeneration. *Cell. Mol. Life Sci.* **71**, 1607–1622
17. Adeniyi, P., Gong, X., MacGregor, E., Degener-O'Brien, K., McClendon, E., Garcia, M., *et al.* (2023) Ferroptosis of microglia in aging human white matter injury. *Ann. Neurol.* **94**, 1048–1066
18. Jiao, L., Li, X., Luo, Y., Wei, J., Ding, X., Xiong, H., *et al.* (2022) Iron metabolism mediates microglia susceptibility in ferroptosis. *Front. Cell. Neurosci.* **16**, 995084
19. Liu, N., Yu, W., Sun, M., Li, X., Zhang, W., and Wang, M. (2024) Dabrafenib mitigates the neuroinflammation caused by ferroptosis in experimental autoimmune encephalomyelitis by up regulating Axl receptor. *Eur. J. Pharmacol.* **973**, 176600
20. Yu, H., Chang, Q., Sun, T., He, X., Wen, L., An, J., *et al.* (2023) Metabolic reprogramming and polarization of microglia in Parkinson's disease: role of inflammasome and iron. *Ageing Res. Rev.* **90**, 102032
21. Ma, B., Day, J., Phillips, H., Slootsky, B., Tolosano, E., and Doré, S. (2016) Deletion of the hemopexin or heme oxygenase-2 gene aggravates brain injury following stroma-free hemoglobin-induced intracerebral hemorrhage. *J. Neuroinflammation* **13**, 26
22. Da Silva, F., Cordeiro, R., de Carvalho Lima, C., Cardozo, P., Vasconcelos, G., Monte, A., *et al.* (2023) Sex and the estrous-cycle phase influence the expression of G protein-coupled estrogen receptor 1 (GPER) in schizophrenia: translational evidence for a new target. *Mol. Neurobiol.* **60**, 3650–3663
23. Yang, L., Lu, L., Yue, J., Wang, X., Qi, J., Yang, F., *et al.* (2021) Activation of microglial G-protein-coupled receptor 30 protects neurons against excitotoxicity through NF-κB/MAPK pathways. *Brain Res. Bull.* **172**, 22–30
24. Kubota, T., Matsumoto, H., and Kirino, Y. (2016) Ameliorative effect of membrane-associated estrogen receptor G protein coupled receptor 30 activation on object recognition memory in mouse models of Alzheimer's disease. *J. Pharmacol. Sci.* **131**, 219–222
25. Peng, J., He, Y., He, J., Zhang, J. K., Yu, Z. T., and Xia, Y. (2023) GPR30 agonist G1 combined with hypothermia alleviates cognitive impairment and anxiety-like behavior after subarachnoid hemorrhage in rats. *Brain Behav.* **13**, e3204
26. Chen, J., Zhao, R., Wang, Y., Xiao, H., Lin, W., Diao, M., *et al.* (2024) G protein-coupled estrogen receptor activates PI3K/AKT/mTOR signaling to suppress ferroptosis via SREBP1/SCD1-mediated lipogenesis. *Mol. Med.* **30**, 28
27. Zhang, Y. Q., Sun, T., Zhao, Z., Fu, J., Yang, L., Xu, Y., *et al.* (2024) Activation of GPR30 ameliorates cerebral ischemia-reperfusion injury by suppressing ferroptosis through Nrf2/GPX4 signaling pathway. *Neuromolecular Med.* **26**, 33
28. Bauch, J., and Faissner, A. (2022) The extracellular matrix proteins Tenascin-C and Tenascin-R retard oligodendrocyte precursor maturation and myelin regeneration in a cuprizone-induced long-term demyelination animal model. *Cells* **11**, 1773
29. Wang, Y., Sun, J., Zhu, K., Wang, D., Zhao, X., Zhang, H., *et al.* (2023) Microglial aryl hydrocarbon receptor enhances phagocytic function via SYK and promotes remyelination in the cuprizone mouse model of demyelination. *J. Neuroinflammation* **20**, 83
30. Wang, Q., Liu, J., Zhang, Y., Li, Z., Zhao, Z., Jiang, W., *et al.* (2024) Microglial CR3 promotes neuron ferroptosis via NOX2-mediated iron deposition in rotenone-induced experimental models of Parkinson's disease. *Redox Biol.* **77**, 103369
31. Yang, S., Wang, L., Zeng, Y., Wang, Y., Pei, T., Xie, Z., *et al.* (2023) Salidroside alleviates cognitive impairment by inhibiting ferroptosis via activation of the Nrf2/GPX4 axis in SAMP8 mice. *Phytomedicine* **114**, 154762
32. Heurtaux, T., Bouvier, D. S., Benani, A., Helgueta Romero, S., Frauenknecht, K. B. M., Mittelbronn, M., *et al.* (2022) Normal and pathological NRF2 signalling in the central nervous system. *Antioxidants* **11**, 1426
33. Zimmer, T., David, B., Broekaart, D., Schidlowski, M., Ruffolo, G., Korotkov, A., *et al.* (2021) Seizure-mediated iron accumulation and dysregulated iron metabolism after status epilepticus and in temporal lobe epilepsy. *Acta Neuropathol. Commun.* **142**, 729–759
34. Rui, T., Wang, H., Li, Q., Cheng, Y., Gao, Y., Fang, X., *et al.* (2021) Deletion of ferritin H in neurons counteracts the protective effect of melatonin against traumatic brain injury-induced ferroptosis. *J. Pineal Res.* **70**, e12704
35. Shen, K., Reichelt, M., Kyauk, R., Ngu, H., Shen, Y., Foreman, O., *et al.* (2021) Multiple sclerosis risk gene Mertk is required for microglial activation and subsequent remyelination. *Cell Rep.* **34**, 108835
36. Tangirala, R., Jerome, W., Jones, N., Small, D., Johnson, W., Glick, J., *et al.* (1994) Formation of cholesterol monohydrate crystals in macrophage-derived foam cells. *J. Lipid Res.* **35**, 93–104
37. Klinkner, A., Waites, C., Kerns, W., and Bugelski, P. (1995) Evidence of foam cell and cholesterol crystal formation in macrophages incubated with oxidized LDL by fluorescence and electron microscopy. *J. Histochem. Cytochem.* **43**, 1071–1078
38. Cao, Q., Chen, J., Zhang, Z., Shu, S., Qian, Y., Yang, L., *et al.* (2023) Astrocytic CXCL5 hinders microglial phagocytosis of myelin debris and aggravates white matter injury in chronic cerebral ischemia. *J. Neuroinflammation* **20**, 105
39. Hazell, G., Yao, S., Roper, J., Prossnitz, E., O'Carroll, A., and Lolait, S. (2009) Localisation of GPR30, a novel G protein-coupled oestrogen receptor, suggests multiple functions in rodent brain and peripheral tissues. *J. Endocrinol.* **202**, 223–236
40. Eichenbaum, H. (2017) On the integration of space, time, and memory. *Neuron* **95**, 1007–1018
41. Hirahara, Y., Matsuda, K., Yamada, H., Saitou, A., Morisaki, S., Takanami, K., *et al.* (2013) G protein-coupled receptor 30 contributes to improved remyelination after cuprizone-induced demyelination. *Glia* **61**, 420–431
42. Skuljec, J., Gudi, V., Ulrich, R., Frichert, K., Yildiz, O., Pul, R., *et al.* (2011) Matrix metalloproteinases and their tissue inhibitors in cuprizone-induced demyelination and remyelination of brain white and gray matter. *J. Neuropathol. Exp. Neurol.* **70**, 758–769
43. Chang, A., Staugaitis, S. M., Dutta, R., Batt, C. E., Easley, K. E., Chomyk, A. M., *et al.* (2012) Cortical remyelination: a new target for repair therapies in multiple sclerosis. *Ann. Neurol.* **72**, 918–926
44. Hawley, W. R., Grissom, E. M., Moody, N. M., Dohanich, G. P., and Vasudevan, N. (2014) Activation of G-protein-coupled receptor 30 is sufficient to enhance spatial recognition memory in ovariectomized rats. *Behav. Brain Res.* **262**, 68–73
45. Kim, J., Schalk, J. C., Koss, W. A., Gremminger, R. L., Taxier, L. R., Gross, K. S., *et al.* (2019) Dorsal hippocampal actin polymerization is necessary for activation of G-protein-coupled estrogen receptor (GPER) to increase CA1 dendritic spine density and enhance memory consolidation. *J. Neurosci.* **39**, 9598–9610
46. Zhang, C., Liu, Q., Yu, C., Wang, F., Shao, Y., Sun, K., *et al.* (2020) G protein-coupled estrogen receptor 1 knockout deteriorates MK-801-induced learning and memory impairment in mice. *Front. Behav. Neurosci.* **14**, 157
47. Marraudino, M., Carrillo, B., Bonaldo, B., Llorente, R., Campioli, E., Garate, I., *et al.* (2021) G protein-coupled estrogen receptor immunoreactivity in the rat hypothalamus is widely distributed in neurons, astrocytes, and oligodendrocytes, fluctuates during the estrous cycle, and is sexually dimorphic. *Neuroendocrinology* **111**, 660–677
48. Xu, T., Liu, C., Deng, S., Gan, L., Zhang, Z., Yang, G., *et al.* (2023) The roles of microglia and astrocytes in myelin phagocytosis in the central nervous system. *J. Cereb. Blood flow Metab.* **43**, 325–340

49. Gudi, V., Gingele, S., Skripuletz, T., and Stangel, M. (2014) Glial response during cuprizone-induced de- and remyelination in the CNS: lessons learned. *Front. Cell. Neurosci.* **8**, 73
50. Liu, C., Zhang, N., Zhang, R., Jin, L., Petridis, A. K., Loers, G., *et al.* (2020) Cuprizone-induced demyelination in mouse Hippocampus is alleviated by ketogenic diet. *J. Agric. Food Chem.* **68**, 11215–11228
51. Song, N., Wang, J., Jiang, H., and Xie, J. (2018) Astroglial and microglial contributions to iron metabolism disturbance in Parkinson's disease. *Biochim. Biophys. Acta, Mol. Basis Dis.* **1864**, 967–973
52. Ryan, S., Zelic, M., Han, Y., Teeple, E., Chen, L., Sadeghi, M., *et al.* (2023) Microglia ferroptosis is regulated by SEC24B and contributes to neurodegeneration. *Nat. Neurosci.* **26**, 12–26
53. Qu, Y., Li, N., Xu, M., Zhang, D., Xie, J., and Wang, J. (2022) Estrogen upregulates iron transporters and iron storage protein through hypoxia inducible factor 1 alpha activation mediated by estrogen receptor β and G protein estrogen receptor in BV2 microglia cells. *Neurochem. Res.* **47**, 3659–3669
54. Gao, T., Dong, L., Qian, J., Ding, X., Zheng, Y., Wu, M., *et al.* (2021) G-Protein-Coupled estrogen receptor (GPER) in the rostral ventromedial medulla is essential for mobilizing descending inhibition of itch. *J. Neurosci.* **41**, 7727–7741
55. Shao, Y., Ding, J., He, Q., Ma, Q., Liu, Q., Zhang, C., *et al.* (2020) Effect of Sox10 on remyelination of the hippocampus in cuprizone-induced demyelinated mice. *Brain Behav.* **10**, e01623